Wall pressure and external velocity field relation in over-expanded supersonic jets

V. Jaunet, S. Arbos, G. Lehnasch, S. Girard

Wall pressure and external velocity field relation in over-expanded supersonic jets

V. Jaunet[*], S. Arbos[† *], G. Lehnasch[*], S. Girard[*],

Truncated Ideal Contour nozzles operating at off-design conditions encounter off-axis loads whose exact origin remains unclear. While these loads are usually attributed to non-axisymmetric motion of the adaptation shock wave, the unsteady pressure field in the downstream separated region may also be of importance: as the distance from the nozzle's structural attachment increases, small wall pressure fluctuations can generate undesired torque. Experiments are conducted on a Truncated Ideal Contour nozzle operated at over-expanded conditions. The study investigates the unsteady characteristics of the pressure fluctuations in the downstream separation region, and their links with the downstream developing jet flow dynamics. The analysis of the pressure fluctuations inside the nozzle reveals the existence of highly organized structures, both in time and in the azimuthal direction. It is shown that these organized fluctuations dominate the pressure signals in the separation region and that they correspond to an azimuthal mode responsible for the side-load generation. Moreover, it is shown that these specific pressure modes have a clear signature in the exiting jet flow field. A discussion is given in the paper on the possible origins of these organized structures.

[*]Institut PPRIME, UPR-CNRS-3346, Université de Poitiers, ENSMA, France
[†]CNES Direction des Lanceurs, Paris

Nomenclature

L	=	Nozzle length
D	=	Nozzle exit diameter
$\mathbf{x}$	=	Position vector
U	=	Streamwise mean flow velocity
V	=	Vertical mean flow velocity
M	=	flow Mach mumber
p	=	wall pressure
$\cdot_j$	=	subscript referring to the fully expanded jet parameters
St	=	Strouhal number
m	=	azimuthal mode number
ω	=	pulsation
k	=	wavenumber
ϕ	=	phase shift
V_ϕ	=	phase velocity
C	=	time-domain correlation function
$\hat{C}$	=	cross-spectral density function
$\hat{H}$	=	frequency domain transfer function
γ	=	coherence function

I.   Introduction

In recent years there has been an increasing interest in improving the performance of rocket engines. One of the main design challenges encountered in their optimization is to accurately predict the aerodynamic forces inside the nozzles during the start-up phase. The prediction of these forces is of critical importance since they can generate off-axis loads that can severely compromise the nozzle integrity. During this start-up phase the nozzle is said to operate under an *over-expanded* regime. This regime is characterized by oblique shocks emanating into the flow-field to adapt the exhaust flow to the ambient pressure. Further downstream, a system of shocks and expansion waves leads to the characteristic shock pattern in the exhaust plume [26]. During this operational regime, large structural asymmetric forces referred to as *side-loads* take place. These forces can cause severe damage to the engine, the nozzle and even the payload [20]. The study by Nave and Coffey [20] also described that two flow separation regimes exist for over-expanded nozzles: *Free Shock Separation, FSS* and *Restricted Shock Separation, RSS*. The occurrence of these flow patterns depends on the nozzle geometry. Truncated Ideal Contour, TIC, and conical nozzles only display FSS separation regimes while Thrust Optimized Contour, TOC, and Thrust Optimized Parabolic, TOP, nozzles can display both FSS and RSS regimes depending on the nozzle pres-

American Institute of Aeronautics and Astronautics

sure ratio [27]. Since the early work of Schmucker [37], it is commonly suggested that side loads in the FSS regime mainly result from oscillations of the internal shock pattern within the nozzle [11, 20, 27, 1] while in mixed regimes a peak of side-loads is observed for NPR corresponding to the transition FSS-RSS [47, 45, 26]. A detailed description of the classical FSS regime in an over-expanded nozzle can be found in Hagemann et al. [15].

Based on the work of Nave and Coffey [20], Schmucker [36] proposed a detailed analysis of the side-loads mechanism. The study linked appearance of side-loads to an asymmetry of the separation region, which in turn can be either steady or unsteady. As for example, a steady asymmetric flow may be due to several factors such as imperfections in the combustion or manufacturing errors that lead to non-axisymmetric nozzle profile. Schmucker [36] conjectures that the unsteady side-loads are due to small changes in flow properties around its steady behaviour. The study derives a model to predict both steady and unsteady side-loads based on an empirical boundary layer separation criteria and on the observation that most of the pressure fluctuations are located close to the separation point.

Great effort both in academia and in industry has been made into trying to predict these asymmetrical lateral forces; thus, several analytical and empirical prediction methods have been proposed. In particular, a very comprehensive study on the history of separated rocket nozzle flow as well as flow separation prediction methods for convergent-divergent nozzles is given in reference [38]. Nonetheless, these are still approximate and more insight is required in order to generalize them.

More recently, the relation between nozzle geometry and side-load magnitude was analysed through the development of an analytical model [1]. As in the previous studies from Schmucker [37] or Dumnov [11], the model assumes that the FSS-induced side-loads are caused by asymmetric oscillations of the internal separation shock. Moreover, the dynamics of the shock oscillation are obtained through a spring-damper system. The coefficients of the system are identified using analytical models of the boundary layer, separation criterion and oblique shock equations. Note that the spring damper analogy presented in the study by Aghababaie and Theunissen [1] is analogous to the model proposed by Plotkin [30]. The latter model was experimentally ascertained by Poggie and Smits [31] and theoretically, in the case of shock-wave boundary layer interaction, by Touber and Sandham [46]. Thereby, suggesting that shock motion in rocket nozzles under FSS regime behaves similarly to that seen in SWBLI. Nevertheless, this is a questionable statement since in FSS regime no reattachment point can be defined.

Hence, it seems well entrenched that FSS-induced side-loads are linked to oscillations of the internal shock pattern within the nozzle. Nonetheless, the role of the pressure fluctuations in the fully separated region, *i.e.* downstream of the separation shock, in the creation of loads is still unknown. Due to its more distant position from the nozzle mounting point compared to the more studied separation region, this part of the nozzle is very inclined to the creation of undesirable

torque which may have a non-negligible impact during the flight. In his early work, Dumnov [11] proposed a side-loads model including both pressure fluctuations due to the motion of the separation shock foot and the pressure fluctuations present in the separated flow region. To derive this model, Dumnov [11] assumed that pressure fluctuations in the separated region are due to the change of pressure-jump across the shock, due to the fact that the shock occurs at varying upstream Mach number depending on its location in the nozzle. However, this did not account for the presence of the turbulent mixing layer that is created by the separation of the incoming boundary layer, where absolute instabilities can form [42, 9]. Baars et al. [4] experimentally investigated the pressure unsteadiness in a TOP nozzle in both FSS and RSS regime and reported that the spectral content of pressure fluctuation in FSS state is dominated by low and high frequency humps, that they associated to shock wave/boundary layer interaction. However, they focused in this study on only four nozzle pressure ratios (NPR) with only one for the FSS regime. Hence, they did not provide a fine description of the wall pressure fluctuation with respect to the NPR in this study. In more recent studies, the same group provided experimental investigation of pressure fluctuations using varying NPR conditions and time-frequency analysis [3, 5]. They therefore were able to scan an entire range of NPR conditions in a single run. The drawback of such approach is that it is difficult and costly to obtain converged statistics. However, one of the great assets of their study is the fact that the authors placed their sensors in azimuthal arrays to isolate the anti-symmetric azimuthal mode, which is the only one responsible for side-loads creation. Previous attemps to isolate this azimuthal mode used only two sensors in the azimuthal direction [9, 19], giving under-sampled data in the azimuthal direction.

Continuing the work of Baars and Tinney [3] and Baars et al. [5], this paper aims at providing insights on the behaviour of the pressure fluctuations and their associated azimuthal Fourier modes. We focus on the separated zone of the flow in a TIC nozzle (FSS regime) providing an analysis of different regimes that can be observed by finely varying the NPR. Moreover, we also want to give information on the existing links between observed pressure unsteadiness with the external jet flow field. The paper firstly focuses on the description of the wall pressure fluctuations in the separated region inside the nozzle: the different regimes that we could observe are characterized. Then, the possible links between these internal pressure dynamics and then external flow field are analyzed through the use of synchronized measurements of velocity fields and wall pressure samples.

II. Experimental arrangement

A. Reduced scale model

The tests presented are conducted at the S150 cold blow down supersonic wind tunnel at Pprime Institute in Poitiers, France. A reduced scale Truncated Ideal Contour Nozzle is considered as it guarantees an FSS separation structure. The TIC nozzle contour is designed using a computational method based on the work of Délery [10]. These include the 2D axisymmetric method of

characteristics and boundary layer correction with an integral method. The obtained shape is then truncated. The exit Mach number of the full flowing flow, based on throat to exit area ratio, is $M_d = 3.5$. A 3D diagram of the nozzle is presented in figure 1. The reference system is chosen so that $x = 0$ at the throat of the nozzle and distances are normalized by the length of the diverging part of the nozzle L.

The exit section of the nozzle is located at more than 15 nozzle exit diameters from the ground. The flow evolves freely until it gets guided to the exterior of the building by a convergent, approximately 35 diameters downstream of the exit section. Hence, no obstacle is located in the flow path ensuring the free evolution of the flow. The nozzle is fabricated in an aluminum alloy with thick walls – the nozzle lip is 0.1 D – ensuring negligible aero-elastic coupling.

The nozzle is supplied with high-pressure desiccated air having a dew point of $200K$. The supplied air is first expanded from a storage pressure, 200 bar, to the desired stagnation pressure. This process is executed using an automated controller that ensures the stability of the nozzle pressure ratio. Hence, the stagnation pressure remains almost constant during a run, with a variation of less than 1%. Before reaching the supersonic nozzle the flow passes through a stagnation chamber of large dimensions, compared to those of the nozzle, equipped with grids to ensure a low turbulence level, typically less than 1%, in the potential flow region.

All the different experiments were conducted at constant NPR. The fully adapted Mach number M_j is retained as the independent parameter to reflect the nozzle operating conditions. This parameter is commonly used in the compressible jet noise community [44, 33] and is believed to be relevant also in this study. The fully adapted Mach number is linked to the NPR via the isentropic relation:

$$\frac{P_e}{P_0} = \left(1 + \frac{\gamma - 1}{2}M_j^2\right)^{-\frac{\gamma}{\gamma-1}}, \tag{1}$$

where γ is specific heat ratio, P_e is the external pressure and P_0 the stagnation pressure, hence P_e/P_0 is the invert of the NPR. Note that in the rest of the paper M_j and NPR will be used to refer to the nozzle operating conditions.

B. Unsteady pressure measurements

The nozzle is equipped with 18 flush-mounted pressure transducers Kulite XCQ-062. The sensor range is of 1.7 bar absolute, and they have a measurement area of 1.7 mm in diameter. The cut-off frequency of the sensors is around 40 kHz, which guarantees a sufficient temporal resolution for this study. Table 1 presents the position of the pressure transducers. It can be seen that at locations $x/L = 0.667$ and $x/L = 0.853$, six transducers are placed equidistantly along the circumference, thus allowing the computation of azimuthal Fourier modes. These two azimuthal arrays are indicated by two white lines in figure 1.

The signal is acquired at a sampling rate of 100 kHz for more that 90 seconds at each run. Since this is more than twice the response frequency of the pressure sensors, spectral aliasing was avoided
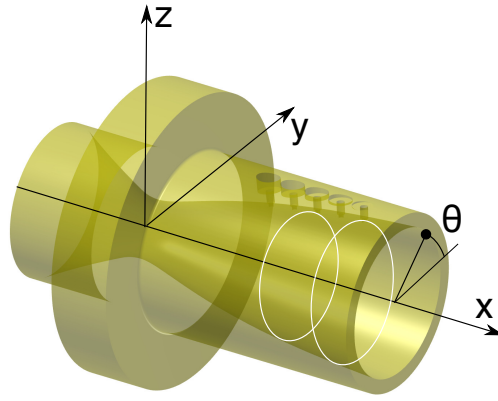
Figure 1. Chosen reference system and presentation of the array of pressure sensors location.

without the need for low-pass analog filters. Fourier analysis of the signals was performed using FFT algorithm and Welch periodogram technique. The vector of pressure samples was divided in blocks of 4096 points providing a resolution of 24Hz, sufficient for the observations of this study. The acquisition was long enough to provide more that 900 non-overlapping blocks of data so that the computed power spectral densities are well converged.

In the following the frequency is presented in terms of Strouhal number, $St = f\frac{D_j}{U_j}$, based on the fully expanded jet velocity U_j and the fully expanded jet diameter D_j. U_j is obtained through the NPR (*i.e.* M_j) and the stagnation temperature T_0:

$$U_j = \sqrt{\gamma r T_0} \frac{M_j}{\sqrt{\left(1 + \frac{\gamma-1}{2}M_j^2\right)}}. \tag{2}$$

D_j is obtained via M_j, the design Mach number M_d and design exit-section diameter D, by the condition of mass flux conservation [44]:

$$\frac{D_j}{D} = \left(\frac{1 + \frac{\gamma-1}{2}M_j^2}{1 + \frac{\gamma-1}{2}M_d^2}\right)^{\frac{\gamma+1}{4(\gamma-1)}} \left(\frac{M_d}{M_j}\right)^{0.5}. \tag{3}$$

C.   PIV measurements

In order to obtain quantitative information of the jet a 2D-2C Particle Image Velocimetry, PIV, system is used whose camera is placed perpendicularly to the flow. The acquisition as well as the initial post-processing analysis is done using a commercial software. The system consisted of two 4 Mpixel CCD cameras equipped with a 105 mm macro lens. The aperture is set at $f\#8$. A Nd:YAG EverGreen Quantel Laser is used delivering light pulses of 200 mJ, sufficient to illuminate the area of interest. The laser sheet is less than 1 mm thick and it is shone from an optic located on top

American Institute of Aeronautics and Astronautics

x/L	N sensors	$\Delta\theta$
0.481	2	π
0.574	2	π
0.667	6	$\pi/3$
0.760	2	π
0.853	6	$\pi/3$

Table 1. Location of the pressure transducers. The first column provide their axial locations, the second column gives the number of azimuthal probe positions at this axial location and the corresponding azimuthal angle between successive probes.

of the jet to minimise the interference and fluctuations caused by the high turbulence and acoustic waves generated by the jet. The obtained Field Of View (FOV) is about 2 nozzle diameters in the $(x, y) - plane$. The PIV was ran at a sampling rate of 2 Hz and the flow was seeded using SiO_2 particles whose mean diameter was estimated to $0.3\mu m$ and their relaxation time to $0.019ms$ [17]. This is sufficient for the time scales of interest in this paper. The flow was seeded internally, via a seeding cane placed inside the resting chamber, and externally, with a seeding cane aligned with the laser plane. It was checked that the flow was not affected by the seeding system by comparing wall pressure measurements with and without the seeding canes.

The initial post-processing was done with decreasing window size 128×128 to 32×32. A total of three passes with a 50% window overlap was used. The first pass was performed using square windows, adaptive PIV algorithm [35] was used thereafter. Vectors are validated using a universal outlier detection [49] together with the standard correlation peak-ratio criterion. Only the validated vectors were used in the following processing stages. The vector fields were filtered to discard the faulty images due to inhomogeneous seeding resulting in an amount of 7800 vector fields. They represent a sufficient number of independent snapshots to converge the relevant statistical quantities studied.

Due to the slow acquisition rate of the PIV system, the PIV experiments were conducted at a single NPR, equivalent to $M_j = 2.09$, which was chosen because at this M_j the wall pressure shows distinct phenomenon that we wanted to study more in detail. The PIV acquisitions were performed such that the PIV snapshots and the pressure measurements were synchronised; hence, allowing the correlation between the internal and the external jet dynamics.

III.   Mean flow field

An overview of the internal flow field in the FSS regime is given in figure 2 where the main shock pattern is represented as well as the separated region. The main flow feature is a flow separation leading to the creation of a shear layer that never reattaches to the wall in this regime. The general evolution of the mean wall pressure is also given in this figure. We see that the pressure

American Institute of Aeronautics and Astronautics

rises quickly across the adaptation shock wave and follows a slow recovery to the external pressure. Beyond the nozzle's exit section, an axisymmetric jet flow is formed and continues to develop downstream.
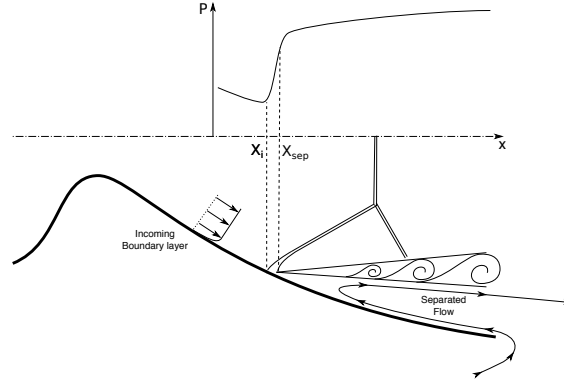
**Figure 2. Geometry of the flow field inside the nozzle in FSS regime.**

The mean wall pressure evolution, normalized by the stagnation pressure P_0, is presented in figure 3 for several stagnation pressure values. Pressure profiles obtained from the generalized free interaction theory of Carriere et al. [6] is also plotted on the same figure. This profile is obtained by solving the following equation:

$$\frac{p(x) - p_i}{q_i} = \frac{C_{fi} F(\bar{x})^2}{\bar{\nu}(x) - \nu(x)} \tag{4}$$

where the subscript i stands for variable at the origin of the interaction. p is the wall pressure and q the dynamic pressure at the boundary layer edge. $\bar{x} = \frac{x - x_i}{l_s}$ is the distance from the origin of the interaction normalized by the interaction length $l_s = X_{sep} - X_i$ (see figure 2). The skin friction coefficient C_{fi} is computed iteratively via the Kármán-Schoenherr equation and compressibility correction. The interaction length is determined from Chapman's expression [7]. We used experimentally obtained separation location x_{sep}, corrected by the interaction length, as the incipient separation location x_i in equation 4. An iterative process was then used to fine-tune both the interaction length and the incipient separation location. ν and $\bar{\nu}$ are the Prandtl-Meyer angles of the flow with and without interaction respectively.

We present in figure 3 a comparison of the wall pressure profiles obtained via the semi-empirical model and the measurement. Note that the model constants were optimized to obtain a best match through the entire range of NPR experimentally investigated. It is clear that the experimental observations can correctly be represented by this widely used model showing that the current data is consistent with the results that can be found in the literature.

A comparison of the current separation location with a selected number of separation criteria [51, 36, 41, 40] is given in figure 4. Note that we measured the separation point location using oil flow visualization. This estimated separation location is found slightly downstream (at a lower

American Institute of Aeronautics and Astronautics
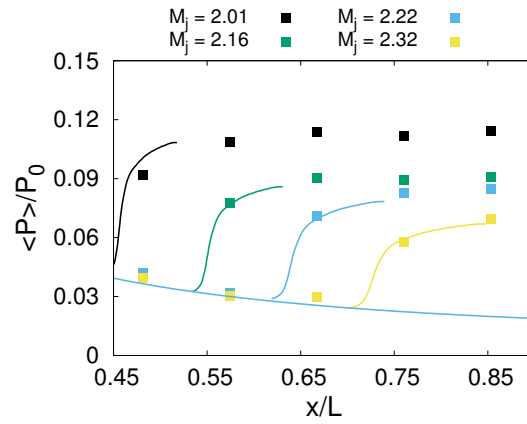
Figure 3. Mean wall pressure evolution along the x-axis for various M_j. The symbols correspond to measured data points, the lines correspond to the free interaction theory [6].

P_e/P_a) than the different predictions. This shift might be expected since different criteria are used to educe the location of the separation point. In the present case, it was directly estimated by visualizing the upstream limit of the trace of oil initially put at the downstream nozzle wall. This criterion differs from Stark [41], for example, where this separation point is inferred from pressure signals only, by extrapolating the line of maximal slope in the region of pressure rise. The criteria used in figure 4 were also derived for higher Mach number and/or turbulent incoming boundary layer. Since the Mach numbers of the present study remain relatively moderate, the use a laminar separation criterion might also lead to more precise prediction [39].

Nevertheless, it is worth precising that these criterion are also obtained using data coming from different flow fields, and various experiments with different boundary conditions. The scatter in the data used by Stark [41] can be circumscribed using the criterion he proposed $\pm20\%$. It leads to consider a rather large uncertainty zone, indicated by asterisks symbols in figure 4. We clearly see that the current data is also contained in between the reported limits. It confirms that the present nozzle flow globally behaves similarly to other overexpanded separated flow in FSS regime.

We present in figure 5 the mean external flow measured by PIV for $M_j = 2.09$, normalized by the fully expanded jet velocity U_j. We see from the streamwise component that the maximum velocity is not encountered at the centre of the jet. This is expected because of the presence of a normal shock wave as shown in figure 2, which creates a subsonic jet core whose extent excesses a nozzle diameter. The normal shock observed outside of the nozzle in figure 5, corresponds in fact to a secondary normal shock issued from the replication of the upstream main shock structure. Hence, the exiting mean flow is mainly formed by an annular shaped high velocity region, that is modulated in amplitude by a complex series of compression and expansion waves, more visible in the vertical component in figure 5.

Since performing PIV in such a complex flow field is always challenging, we provide in figure 6 a comparison of the mean velocity profiles obtained by either PIV or Triple probe measurements

American Institute of Aeronautics and Astronautics
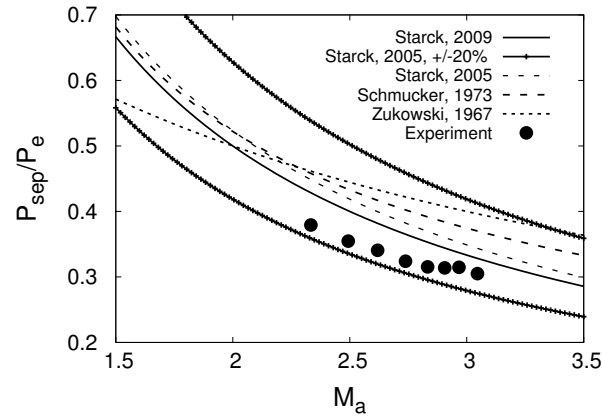
Figure 4. Comparison of experimental and predictions of incipient separation wall pressure normalized by the external pressure P_{sep}/P_e as function of incipient separation Mach number M_a.
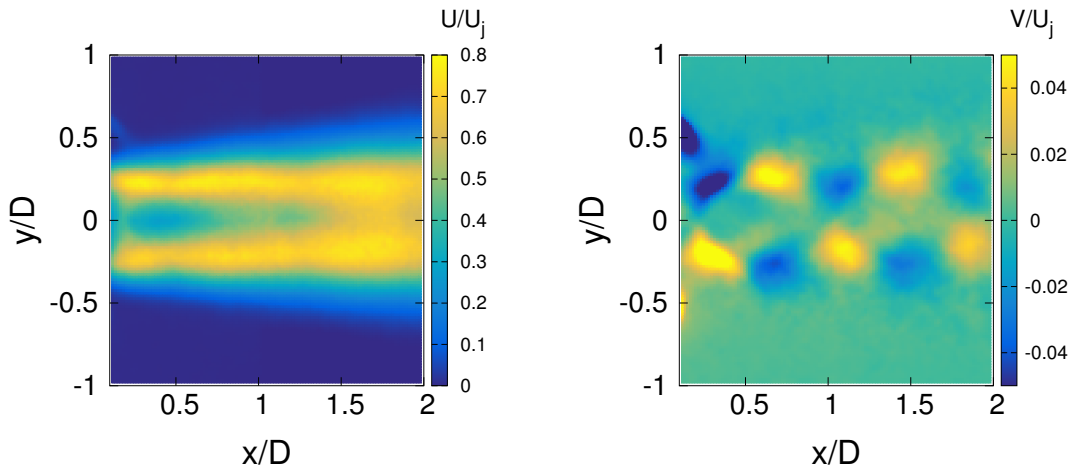
Figure 5. Mean flow measured by PIV for $M_j = 2.09$, streamwise velocity (left), vertical velocity (right).

(stagnation pressure, stagnation temperature and static pressure). As can be seen there is a reasonable agreement between the two measurement techniques, ensuring that the PIV set-up correctly retrieved the essential features of the flow field.

In the following we present the unsteady pressure field and extract its main features. Then we try to identify the possible links between the external velocity fluctuations and the main modes of internal pressure.

American Institute of Aeronautics and Astronautics
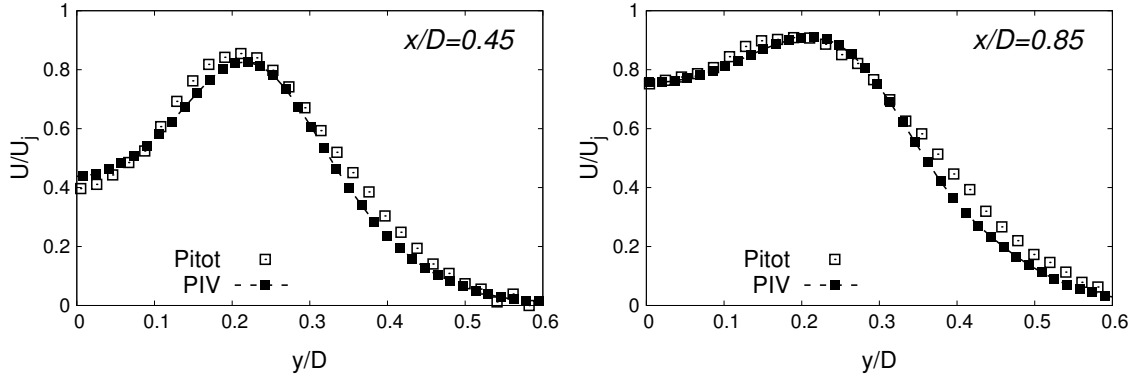
Figure 6. Comparison of velocity profiles obtained with PIV and triple probe (static and total pressure and total temperature). The measurement is taken at $x/D = 0.45$ **(left) and** $x/D = 0.85$ **(right) for** $M_j = 2.09$**.**

IV.   Unsteady wall pressure field

A.   Evolution of the pressure PSD along axis

The Power Spectral Densities (PSD) of the pressure fluctuations are defined as the Fourier transform of their auto-correlation function:

$$< pp^* > (\omega) = \int_{-\infty}^{\infty} \langle p(t)p^*(t + \tau) \rangle \, e^{-i\omega\tau} d\tau, \tag{5}$$

where $< \cdot >$ is the average operator, $\omega = 2\pi f$ is the pulsation and $\cdot^*$ refers to the complex conjugation. We plot in figure 7 the Power Spectral Densities of the pressure at all measured axial location for $M_j = [1.83 - 2.09 - 2.27]$, where M_j is the fully expanded Mach number of the jet. The PSDs are arbitrarily plotted with a Strouhal number based on the fully expanded jet diameter D_j and the exit velocity of the fully expanded jet U_j. The PSDs are presented in a pre-multiplied form and are normalized by the dynamic pressure of the fully expanded jet $\gamma P_j M_j^2$.

At $M_j = 1.83$, all the sensors are located downstream of the separation. From figure 7 (top) we can see that the spectrum consists in a very low frequency hump ($St < 0.1$) whose amplitude and dominating frequency remains constant in the streamwise direction. Another broadband hump can be observed for $0.1 < St < 0.2$. This peak has increasing amplitude and main frequency with increasing axial location. Then, at moderate Strouhal number $0.2 < St < 0.7$, we observe a series of distinct peaks whose frequency seems constant over the x-axis but whose amplitude is not monotonic in this direction. At higher Strouhal numbers, a third hump can be observed whose energy globally increases with the axial position while its main frequency decreases. This behaviour might be interpreted as the signature at the wall of the developing mixing layer: with increasing axial location the mixing layer thickens, the turbulent scales grow lowering the dominating frequency. These observations are very similar to what Baars et al. [4] reported in the FSS regime in a TOP nozzle.
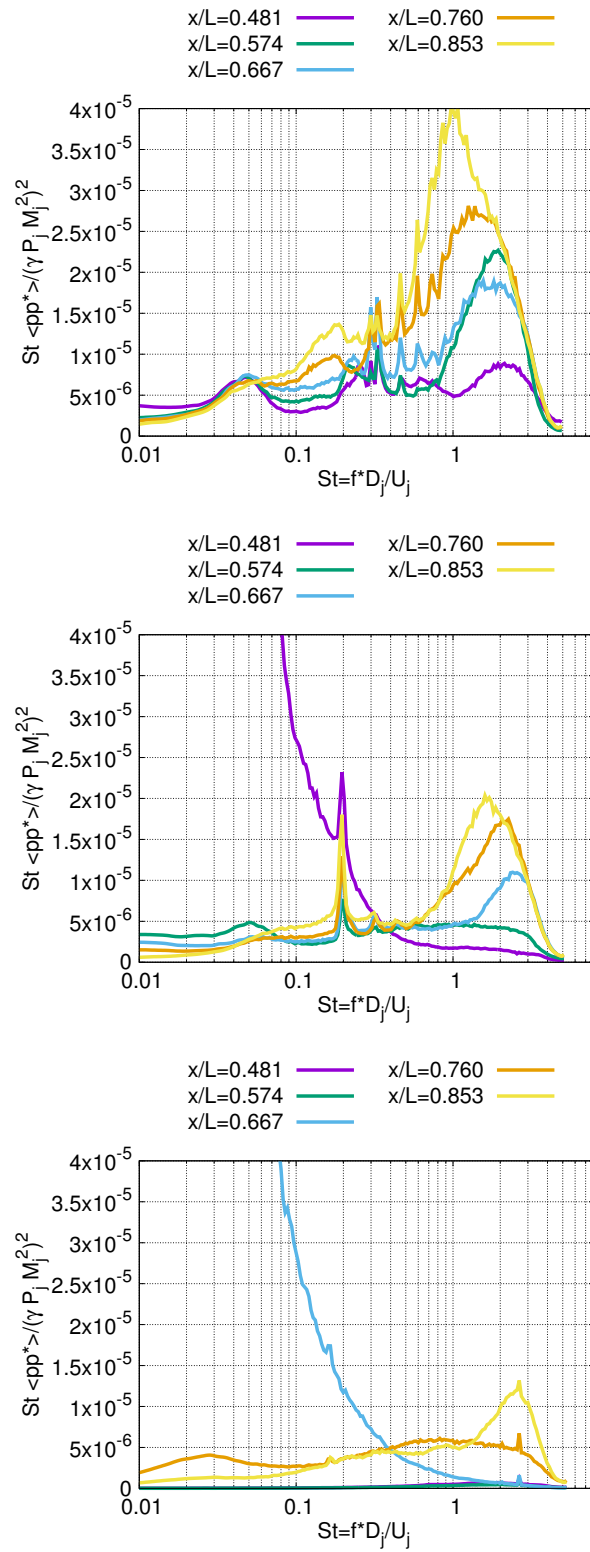
Figure 7. PSD of the pressure as function of Strouhal number at all measured axial location for $M_j = 1.83$ **(top),** $M_j = 2.09$ **(middle),** $M_j = 2.27$ **(bottom).**

American Institute of Aeronautics and Astronautics

Note that a careful look at the energy level for this hump puts into evidence that the energy does not always only evolve in a monotonic way with the downstream direction. Indeed, at $M_j = 1.83$, the pressure fluctuation energy appears lower at x/D=0.667 than at the previous location $x/D = 0.574$, before increasing again in the downstream direction. This suggests the presence of additional pressure fluctuations within the jet, which contribute to the energy content for this higher frequency range. We might suspect in particular a non-negligible role of shock-mixing layer interactions, which are likely to enhance the level of pressure fluctuations measured at the nearest probes at the wall. It is yet not possible from the current experiment to fully explain this behavior.

At $M_j = 2.09$, see figure 7 (middle), all the sensors are located downstream of the separation except the first one, which is located within the intermittent separation zone. The PSD of this sensor is dominated by very low-frequency content which is the signature of the shock motion, as reported in the case of shock-wave/boundary layer interactions [12, 29, 8]. The overall evolution of the other PSDs is similar to the $M_j = 1.83$ case: low and high frequency humps are still observable. However, in the middle frequency range, the numerous distinct peaks observed at $M_j = 1.83$ are no longer visible at $M_j = 2.09$. Instead, there is only one strong and very distinct peak at $St = 0.2$. Smaller ones that are not harmonics follow this peak. Appearance of such peaks was also reported in numerous studies of convergent-divergent nozzles and are usually attributed to screech or transonic resonance mechanism [50, 21, 4, 3, 14, 5, for instance]. This specific question is addressed later in this paper.

At $M_j = 2.27$, see figure 7 (bottom), two sensors are located upstream of the separation shock wave ($x/L = 0.481$ and $x/L = 0.574$). They therefore measure pressure fluctuations in the incoming boundary layer, which are expected to be dominated by frequencies higher than the cut-off frequency of the transducers. This explains why we do not obtain any contribution with respect to the frequency content of their respective signals. As can be seen in figure 7 (bottom), at $M_j = 2.27$ the sensor located at $x/L = 0.667$ shows a spectrum largely dominated by low frequency content, typical signature of the intermittent passage of the separation shock wave above the transducer. This is similar to the observation made at $M_j = 2.09$ for the first sensor. This shows the forward displacement of the shock wave when the NPR in increased. Regarding the separated region of the flow, we only have two sensors in this region, but we can see that a high frequency ($St > 1$) peak starts to emerge with the downstream distance. This may again be attributed to the developing mixing layer, and is a common feature of the pressure fluctuations in the separated flow regardless of the fully adapted jet Mach number. However, at this NPR, no distinct peak is observed in the spectrum.

To summarize, we have seen that the pressure fluctuations in the separated flow shows some common features regardless of the NPR especially at low ($St < 0.1$) and high ($St > 1$) frequencies. In contrast, the middle frequency region shows some differences when M_j is varied: at

low M_j a series of very distinct peaks can be observed that has, to the authors' knowledge, never been reported. At slightly higher NPR ($M_j \simeq 2.09$) one single very distinct and energetic peak is visible in the pressure PSD which disappears at higher NPR. This peak seems similar to those previously reported in similar nozzle configurations [4, 3, 21, 14]. Baars et al. [4], Baars and Tinney [3], Georges-Picot et al. [14] and Baars et al. [5] attributed the emergence of such a peak to a transonic resonnance occurring in the nozzle whereas Nguyen [21] recognised these events to be screech tones, usually encountered in supersonic jets [32, 33].

Before discussing this question, we aim at describing in more details the structure on the fluctuating pressure field in the separated region. In the following we present the analysis of the azimuthal modes of pressure with the help of the two azimuthal rings of sensors placed on the nozzle wall.

B. Azimuthal Decomposition of the pressure field

As two azimuthal arrays of sensors are positioned in the nozzle at $x/L = 0.667$ and $x/L = 0.853$, the pressure field at these locations can be decomposed into azimuthal Fourier modes $p_m(x, t)$:

$$p_m(x, t) = \frac{1}{2\pi} \int_0^{2\pi} p(x, \theta, t) e^{im\theta} d\theta, \tag{6}$$

where m is the azimuthal mode number. This decomposition is useful to isolate the pressure fluctuations correlated in the azimuthal direction, for instance the axisymmetric mode $m = 0$, *i.e.* the breathing mode, corresponds to fluctuations of same amplitude, at a given instant t, along the azimuthal direction. By symmetry considerations, it is straightforward to show that only the antisymmetric modes $m = \pm 1$ contribute to the side forces. This is made clearer in figure 8, where an illustration of the four first azimuthal pressure modes is given. In this figure, the grey circle represents the nozzle wall at a given axial position and the arrows represent the force induced by a specific pressure mode on a surface element.

Hence, the decomposition of the pressure field in azimuthal Fourier modes is a necessary tool to identify the sources of side loads [9, 4, 3, 5].
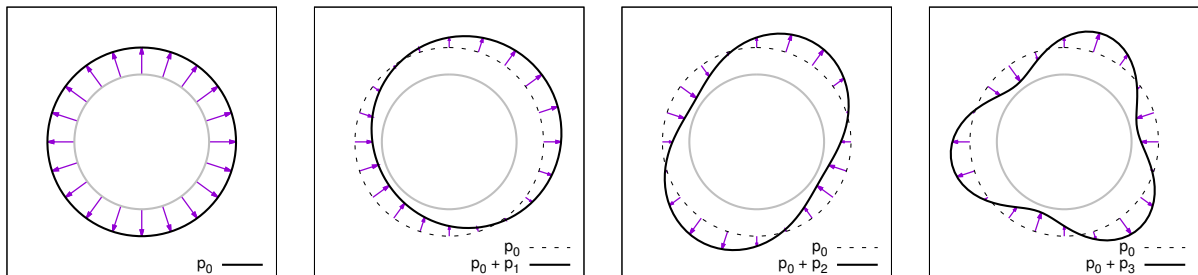
Figure 8. Illustration of the three first azimuthal pressure modes p_m, from left to right: p_0, p_1, p_2 and p_3. The grey circle represents the wall of the nozzle at a given axial position. The arrows represent the force induced by a specific pressure mode on a surface element of the nozzle wall. The azimuthal modes are represented with an arbitry azimtuhal phase shift of $\pi/3$.

The PSD of each individual azimuthal mode can be obtained as the Fourier transform of their auto-correlation function:

$$< p_m p_m^*(x, \omega) > = \int_{-\infty}^{+\infty} \langle p_m(x, t) p_m^*(x, t - \tau) \rangle e^{-i\omega\tau} d\tau \tag{7}$$

We present in figures 9 the PSD of the three first azimuthal modes for $M_j = 1.83, 2.09$ and 2.27 respectively, taken at $x/L = 0.667$.

From figure 9, we can see that the features observed in the previous section are in fact clearly organized in the azimuthal direction. Hence, the low frequency bump ($St < 0.1$) is almost entirely contained in the axisymmetric mode. Different modes contribute to the middle frequency peaks, the strongest mode being associated to the axisymmetric mode and the second highest being mode 1. Higher order peaks also sign on individual modes but no clear harmonic relation can be observed. For frequencies higher than $St = 1$ the azimuthal organization is less clear, each of the modes containing almost the same energy. This observation is consistent with the previous statement that this high frequency broad-band peak is mostly associated with turbulent stochastic structures radiating pressure from the mixing layer.

At $M_j = 2.09$ (figure 9), the same trends can be observed except that the highest peak now signs entirely on the azimuthal mode 1. And the fewer other peaks are contained in mode 2.

At $M_j = 2.27$ (figure 9), the picture is different, as expected from the fact that the pressure sensors are underneath the shock wave at this NPR. The PSDs of all the azimuthal modes are therefore largely dominated by low frequencies and even if the axisymmetric mode is dominating the spectrum, the other higher order modes have a non-negligible contribution to the pressure fluctuations here.

Several conclusions can be made from the latter observations. First of all, the low frequency bump in the detached region of the flow is mostly axisymmetric, and therefore does not contribute to side-loads.

The middle frequency peaks are shown to be very organized in the azimuthal direction, each one of them clearly signing on a preferred azimuthal mode. At $M_j = 2.09$, the strongest peak is actually entirely contained in the azimuthal mode 1, which is the only mode that can contribute to off-axis loads. It must be noticed that no harmonic relation can be found in between the numerous peaks observed in the current results, indicating that the underlying behavior of the jet at those frequencies are independent.

Finally, the signature of the shock moving back and forth over the pressure transducer does not put forward any clear azimuthal organization. This observation suggests that the shock motion is rather stochastic as it is generally observed in two-dimensional shock-wave boundary layer interaction [12, 29, 34, 30, 46] and that the emergence of the peaky azimuthal mode 1 has a different origin from only the shock motion. Note that the same observations can be drawn when looking at the data from the downstream azimuthal array of sensors.
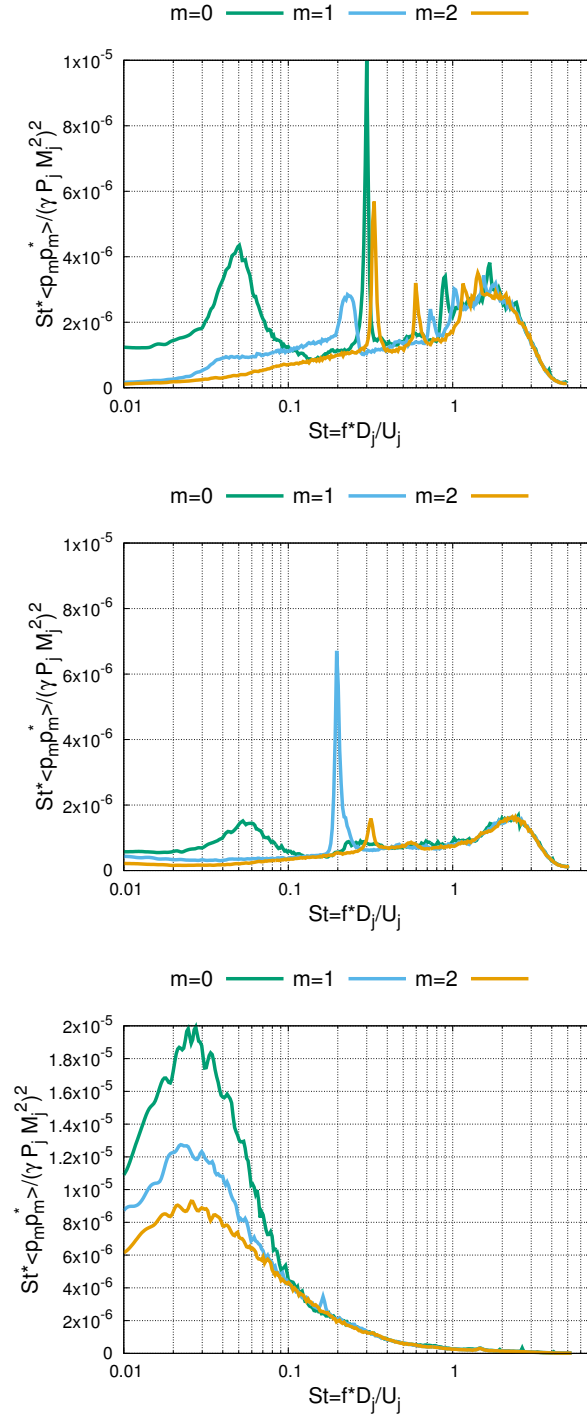
Figure 9. PSD of the 3 first pressure azimuthal modes as function of Strouhal number at $x/L = 0.667$ **for** $M_j = 1.83$ **(top),** $M_j = 2.09$ **(midldle),** $M_j = 2.23$ **(bottom).**

C. Evolution of the PSDs in the (M_j, St) plane

In order to obtain a refined view of the phenomenon, we present in the following figures iso-contours of PSD in the (M_j, St) plane. The iso-contours of the PSD of the axisymmetric mode are first presented in figure 10 for the two measured axial positions. This representation gives more

American Institute of Aeronautics and Astronautics

insights on the behaviour of the pressure fluctuation with increasing NPR. The low frequency bump $St < 0.1$ has a decreasing amplitude with M_j and almost disappears when the shock wave approaches the measured location. The fact that the measurement position is fixed in space makes it difficult to know if this trend is due to the evanescence of the fluctuations with M_j or due to the fact the separation line is closer to the sensor. Since at $M_j = 1.6$ the separated layer is far from the sensor, some instabilities have time to grow before being captured by the sensor. When M_j is increased, the separation moves closer to the sensor and the same instabilities might not have sufficient space to develop in the same manner. This would explain why this low frequency hump shows decaying amplitude with M_j. Furthermore, at the same M_j the low frequency hump is not clearly seen with the downstream azimuthal ring, suggesting that these fluctuations have decaying amplitude in space. This is supported by the results of figure 7 even though the pressure signals are decomposed in azimuthal modes in those results.

Concerning the middle range peaks for $St < 1$, we clearly see that their amplitude is also strongly space dependent: some of them are visible on the second array, but not in the first one. We can also confirm from this figure that the high frequency hump gains energy with the downstream distance while lowering in frequency. This trend is visible for all NPRs comforting the idea that the associated perturbations can be attributed to the developing mixing layer.

The shock passage can clearly be observed around $M_j = 2.3$, where the PSD is dominated by low frequencies at the first measuring positions.
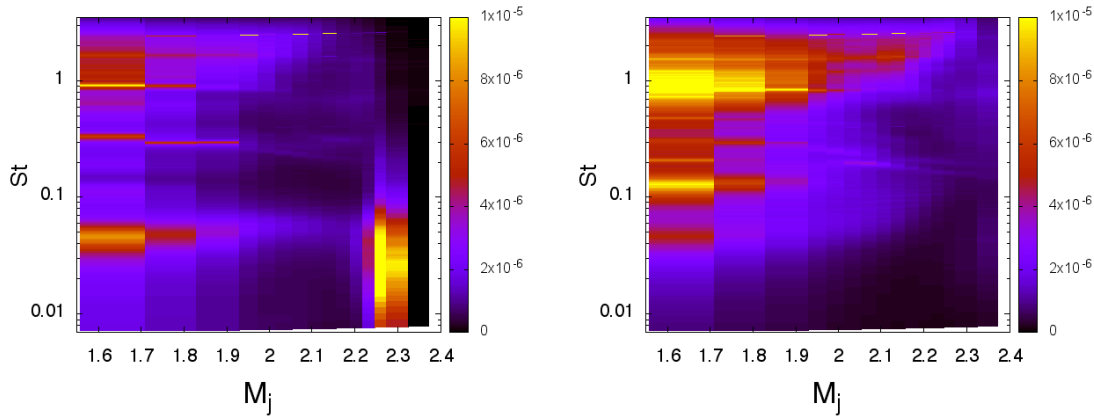
Figure 10. Iso-countours of PSD for the axisymmetric mode m=0: $x/L = 0.667$ **(top) and** $x/L = 0.853$ **(bottom).**

The PSD map of the second azimuthal mode $m = 1$ is presented in figure 11. The previous observations concerning the middle and high frequency range can also be made for the azimuthal mode 1. The difference here concerns the strong peak that was observed at $M_j = 2.09$. It is observable in both measurement locations with almost the same amplitude. Interestingly, the existence of this peak is confined in a very narrow range of M_j and its frequency is slightly decreasing with M_j.

The previous results give insights regarding the pressure fluctuation structure in the separated

American Institute of Aeronautics and Astronautics
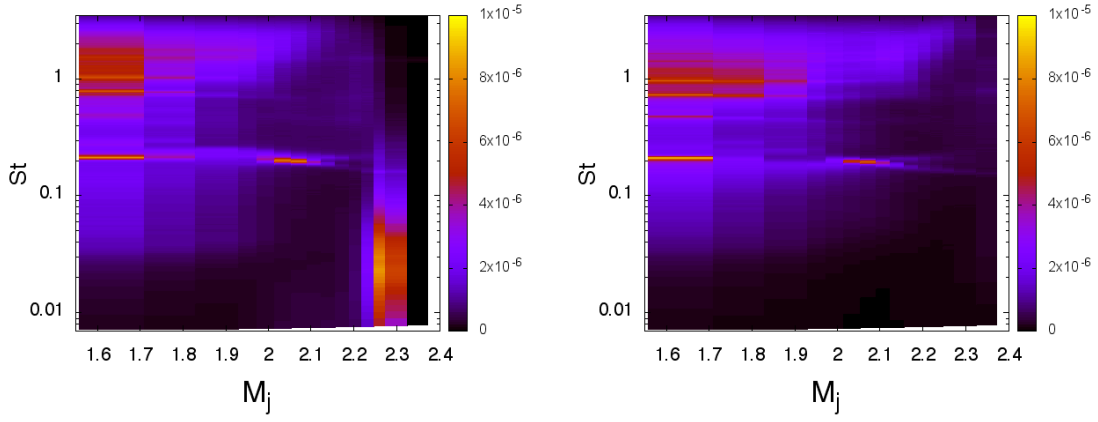
Figure 11. Iso countours of PSD for m=1 and $x/L = 0.667$ **(left) and and** $x/L = 0.853$ **(right).**

region of the flow. The perturbations are strongly space dependent, some are evanescent, some are amplified, depending on the frequency range of interest. In the following paragraph, we want to provide more details about the isolated peak observed at $M_j = 2.09$.

V.   Isolated peak in the wall pressure spectrum

A.   Screech or Transonic Resonance ?

In this section we want to compare the peak at $M_j \simeq 2.09, St \simeq 0.2$ observed in the present investigation with known resonance mechanisms such as screech tones [32, 33, 28, 22, 44] or transonic tones [50, 18].

The transonic resonnance, described by Zaman et al. [50], is observed in C-D nozzles at very low NPR and is due to the excitation of acoustic modes of the nozzle. According to Zaman et al. [50], transonic resonnance only exists when a shock wave lies in the vicinity of the throat. A characteristic of this phenomenon is that the resonnance frequency, and its harmonics, increases with the NPR. This is due to the reducing length in between the shock and the exit section of the nozzle. Zaman et al. [50] provide an empirical prediction formula:

$$St_{tr} = f_{tr}\frac{D_j}{U_j} = C_1(\theta) + mC_2(\theta)(M_j - 1)\frac{a_0}{U_j}\frac{D_j}{L}, \tag{8}$$

where m is the stage number (transonic resonance shows harmonics), $C_i(\theta)$ are empirical functions of the conical angle of the nozzle θ provided by Zaman et al. [50], a_0 is the ambient speed of sound (taken at 340 m/s in our case). The other terms were already defined previously.

The screech mechanism is a also a kind of aero-acoustic feedback mechanism, which involves downstream propagating disturbances and upstream propagating acoustic waves. A more complete description of the phenomenon can be found in Raman [33]. Using hydrodynamic stability theory and approximating the convective speed of the disturbances to $0.7U_j$, Tam et al. [44] derived an

American Institute of Aeronautics and Astronautics

equation to predict the screech frequency:

$$St_{sc} = f_{sc}\frac{D_j}{U_j} = 0.67(M_j^2 - 1)^{-1/2}\left[1 + 0.7M_j\left(1 + \frac{\gamma - 1}{2}M_j^2\right)^{-1/2}\left(\frac{T_a}{T_0}\right)^{-1/2}\right]^{-1}, \quad (9)$$

where T_a and T_0 are the reservoir and ambient temperature respectively. In the following we used an ambient temperature of $290K$ and a reservoir temperature of $260K$, consistent with what was measured during our experiments, values reported in the respective publications were used otherwise.

We report in figure 12 the occurring Strouhal number of the observed peak as a function of the fully adapted Mach number in the current experiment together with the ones that can be seen in the data of Baars et al. [4], Georges-Picot et al. [14] in TOP nozzles and Nguyen [21] in a different TIC nozzle. Furthermore, we plot on the same graph the theoretical value of the screech tone Strouhal number as derived by Tam et al. [44] and for the first mode of transonic resonance as obtained by Zaman et al. [50].

As opposed to Baars et al. [4], Georges-Picot et al. [14] and Baars et al. [5] conjectures, it is clear from this figure that the observed phenomenon cannot be attributed to transonic resonance, regardless of the nozzle type. Indeed, the transonic resonance occurs at very low NPR and its frequency should increase with M_j [50], which is not what is observed. In addition, we see that almost all the reported peaks seem to collapse onto the Strouhal number prediction of screech resonance. The scatter observed can be due to the fact that different screech modes may be associated with the different experiments involved [13].
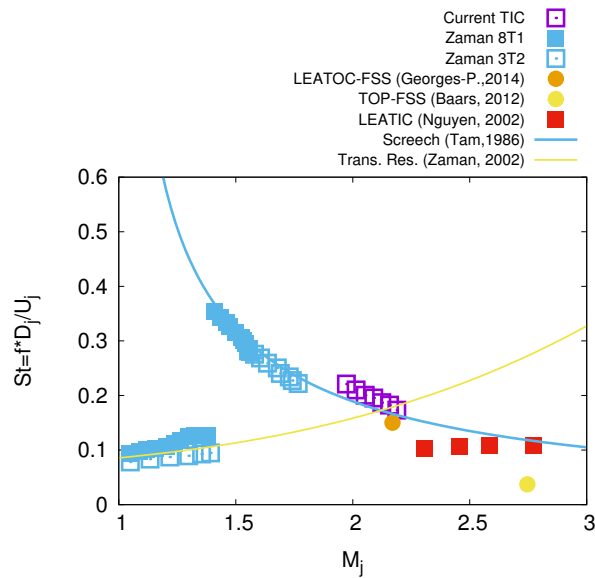

Figure 12. Comparison of current peak Strouhal number with litterature.

Hence, it seems that the observed phenomenon frequency can be predicted using a simple

screech criterion. Furthermore, it seems to collapse data from a variety of different experiments and nozzle suggesting that this phenomenon is geometry independent. This suggests that the peaks in the wall pressure spectrum are due to screech.

Screech is usually accompanied with strong tonal sound waves that should be easily captured with a microphone placed at a distance of $15D$ and at 90 from the jet axis. However, in the current experiment no sign of screech was observed, as can be seen by the absence of visible peaks around $St = 0.2$ for $M_j = 2.09$ in figure 13. Note that the wavy structure of the sound spectrum here presented may be attributed to the lack of acoustic treatment of the wind-tunnel, whose absence should not prevent supersonic jets from screeching.
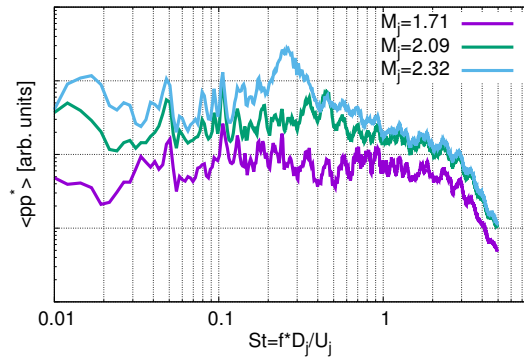
Figure 13. Acoustic pressure PSD measured in the facility for three fully adapted jet Mach number.

In order to further study the link between the internal pressure fluctuations with the acoustic pressure field we compute the coherence $\gamma(St)$ between the microphone signal and the three first azimuthal modes of pressure fluctuations inside the nozzle at $x/L = 0.667$. The results are shown in figure 14. It is clear that the coherence levels are low for all azimuthal modes for St numbers much lower than 1 for both $M_j = 1.71$ and $M_j = 2.09$. Once again, no link can be found between the external acoustic field and the internal peak frequency which contrasts with what is usually observed in screeching jets [2, 48]. On the other hand, we see that the axisymmetric mode of pressure is more coherent with the external acoustic field for high Strouhal numbers, which are associated with mixing layer frequencies.

The previous results are clearly in contradiction with those of figure 12, where the peak frequency was found to collapse well with screech frequency prediction model. This lack of external acoustic signature shows that the observed peaks in C-D nozzle at middle range NPR cannot be entirely associated with a screech resonance, since the acoustic feedback loop is an essential feature of screech mechanism [32]. However, in a classical screech model, the nozzle lip and the the shear layer attached to the nozzle lip are important features of the screech feedback loop. In the current overexpanded jet, the shear layer is initiated by the separation of the incoming boundary layer and the jet starts evolving downstream being enclosed in the surrounding nozzle. Hence, the physics
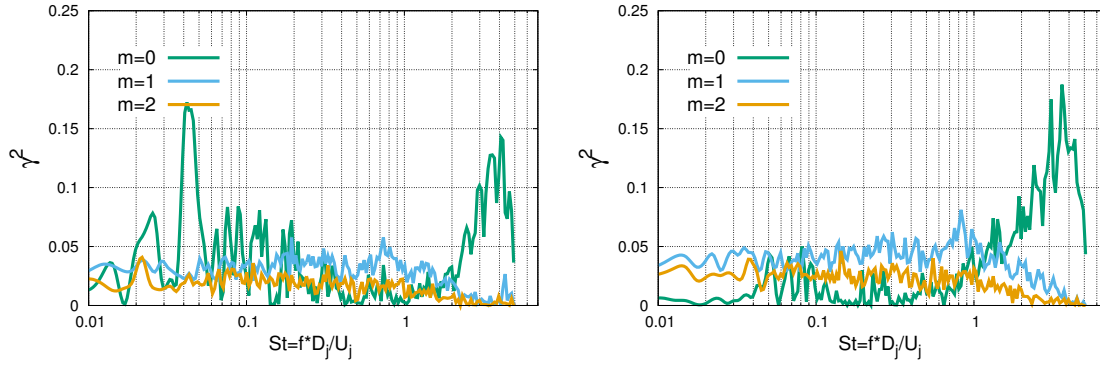
Figure 14. Coherence between external radiated acoustics and internal pressure fluctuations as function of Strouhal number for different azimuthal modes for $M_j = 1.71$ (top) and $M_j = 2.09$ (bottom).

involved in the present study might be different. In view of the particular jet structure, we may also suspect a possible screech-like mechanism whose spatial support would be located within the subsonic jet core surrounded (and hidden) by the supersonic annular mixing region. The fact that the current data follows Tam et al. [44]'s screech theory can be fortuitous and more investigation is required before this question can be answered.

B.   Phase velocity

We have seen previously that in the middle frequency range of the spectrum, the wall pressure signals can contain distinct energetic peaks. Their existence, number and intensity depend on the nozzle working conditions (M_j). At low M_j, numerous peaks can be found in the wall pressure PSD. Increasing the NPR leads to a disappearing of those peaks but in limited range of M_j, strong peaks in PSD can be observed again. Moreover, one single azimuthal mode number can describe each of these peaks. To further complement the description of these tonal modes, we plot in figure 15 the measured phase speed along the x-axis as a function of Strouhal number. The phase speed V_ϕ was obtained using the simultaneous acquisitions along the streamwise direction:

$$V_\phi = \frac{\omega}{k} = \omega \cdot \left(\frac{\partial \phi}{\partial x}\right)^{-1}, \tag{10}$$

where ϕ is the relative phase to a reference point. The phase is obtained as the argument of the cross-spectral density between the pressure signal of a reference point and another one. We used the sensor located at $x/L = 0.667$, as a reference point. It was checked that the choice of the reference sensor did not change results. This is true only if the reference sensor is not located upstream on the separation. In fact, measurements located upstream of the separation where discarded in the process of phase speed evaluation. $\frac{\partial \phi}{\partial x}$ was obtained by a linear regression of the phase evolution along the x axis.

Note that the maximum plotted Strouhal number in figure 15 has been chosen to respect the

fact that the maximum resolvable wavenumber is rather low due to the low spatial resolution of the measurement: the phase may have turned more than 2π in between the two sensors, leading to errors in the phase gradient estimation.

As can be seen in figure 15 the phase velocity is found negative, *i.e.* towards the upstream direction, for a variety of Strouhal numbers at both $M_j = 1.83$ and $M_j = 2.09$. The Strouhal numbers at which the phase velocity is negative correspond to the peaks observed in the wall pressure PSD (see figure 7). Note that their measured phase velocity is subsonic since the sound speed is larger than $0.65U_j$ in the external surrounding air. This lead us to postulate that these peaks could be associated with the upstream subsonic waves theoretically educed by Tam and Hu [43] using linear stability analysis.

In their analysis, Tam and Hu [43] considered adapted supersonic jets and found that the base
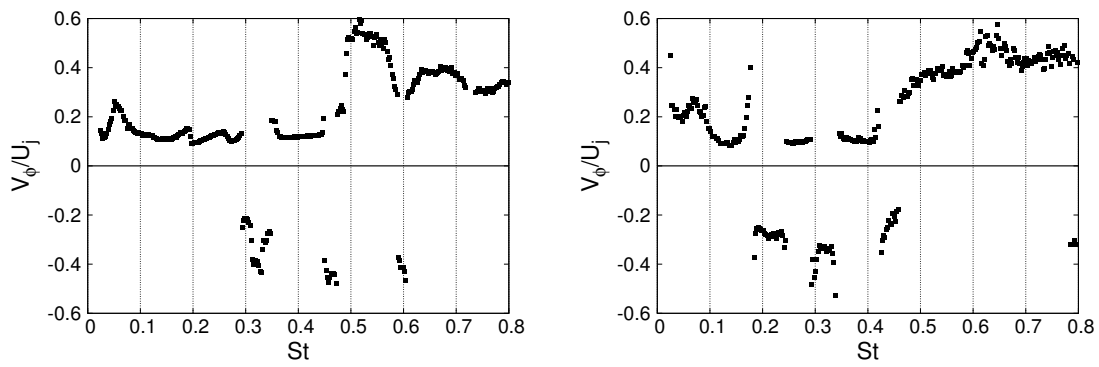
Figure 15. Phase velocity as a function of Strouhal number for $M_j = 1.83$ and $M_j = 2.09$.

flow can support a family of waves having negative phase and group velocities which they labeled *subsonic waves*. For each azimuthal mode, Tam and Hu [43] found a variety of these waves, each of these waves having a very narrow frequency existence. These waves were found to be weakly unstable but have spatial support in the external flow field (this is were our sensors are located with respect to the jet in this study). At that time, they related these waves to the observations of Oertel [23, 24, 25]. Even though the flow of the current study is far from what Tam and Hu [43] considered: presence of wall, non-uniform jet flow field in the axial direction ; all the features they described are surprisingly close to what is observed in the current experiment.

Moreover, it is known from the study of Hu [16] that confinement can play a role in attenuating these waves for the case of rectangular jets. This attenuation depends on the ratio of jet width to the tunnel height. Therefore, the fact the distance from the nozzle wall to the jet flow varies with M_j as the jet separates more and more downstream, could be an explanation why some of the peaks disappear at specific M_j and reappear for a very limited M_j range. This leads us to postulate that the tonal dynamics observed in flow from C-D nozzle may be related to specific instability waves of the jet flow itself.

A key feature of the jet flow of interest in this paper is the existence of an internal subsonic region due to the presence of a normal shock wave (see figure 2). This might give a sufficient support for some internal instability waves to exist with an ability to propagate upstream that could form another type of feedback mechanism. This would explain why the peak frequency can be predicted using jet flow velocity and length scales, as for a screech, without traces of external acoustic feedback. A dedicated study, beyond the scope of this paper would be required to assess the validity of these assumptions.

VI.   External velocity field-internal pressure link

We have seen in the previous section that the pressure fluctuations in the separated region of the internal flow have a rather complex space-frequency behavior. It was also shown that the internal wall pressure fluctuations have a poor signature in the external acoustic pressure. Nevertheless, it is possible that the internal pressure is not fully linked with radiated sound but have signature in the dynamics of jet flowing out of the nozzle. In order to explore this possible link, we analyze the synchronized PIV-pressure measurements described earlier.

For this purpose, we consider the velocity-pressure cross-correlation:

$$C_{up}(\mathbf{x}, \tau) = \int_{-\infty}^{+\infty} u(\mathbf{x}, t) p^*(t + \tau) dt \tag{11}$$

where $\mathbf{x}$ is the location of the PIV samples and $(*)$ denotes the complex conjugate. Since we will focus on the signature of the pressure modes, acquired at a distinct location in the nozzle, into the velocity field we dropped the space dependence of p: $p(t) = p(\mathbf{x}, t)$.

Fourier transforming the cross-correlation gives access to the cross-spectral density (CSD) between pressure and velocity:

$$\hat{C}_{up}(\mathbf{x}, \omega) = \int_{-\infty}^{+\infty} C_{up}(\mathbf{x}, \tau) e^{-i\omega\tau} d\tau, \tag{12}$$

where $\omega = 2\pi f$ is the angular frequency. The CSD alone may be difficult to interpret, thus it is usually preferred to study the coherence function, which is a CSD normalized by the respective power spectral densities (PSD) of the signals:

$$\gamma_{up}^2(\mathbf{x}, \omega) = \frac{\left|\hat{C}_{up}(\mathbf{x}, \omega)\right|^2}{\hat{C}_{uu}(\mathbf{x}, \omega)\hat{C}_{pp}(\omega)} \tag{13}$$

Since we did not use a time-resolved PIV system, the PSD of the velocity is not accessible and the coherence function is therefore not obtainable. However, we have access to the links between pressure and velocity by considering the problem as an input-output system with a transfer function

H. This can be written in the frequency domain as:

$$\hat{u}(\mathbf{x},\omega) = \hat{H}(\mathbf{x},\omega)\hat{p}(\omega). \tag{14}$$

Multiplying both sides of the previous equation by $\hat{p}^*(\omega)$, and taking its average leads to:

$$\hat{H}(\mathbf{x},\omega) = \frac{<\hat{u}(\mathbf{x},\omega)\hat{p}^*(\omega)>}{<\hat{p}(\omega)\hat{p}^*(\omega)>} = \frac{\hat{C}_{up}(\mathbf{x},\omega)}{\hat{C}_{pp}(\omega)} \tag{15}$$

The former equations states that the transfer function from pressure to velocity can be extracted from the ratio of the CSD to the the pressure PSD, which are both accessible from the present database.

As mentioned earlier, the PIV data was obtained using a non time-resolved system. We don't have access to the full time history of velocity samples but only to uncorrelated, distant in time, samples. Nonetheless, an estimate of the pressure-velocity correlation can still be computed using the fact that the pressure signal was obtained continuously, synchronized with the PIV. This estimate is defined in the following way:

$$\tilde{C}_{up}(\mathbf{x},\tau) = \frac{1}{N}\sum_{i=1}^{N} u(\mathbf{x},t_i)p^*(t_i + \tau), \tag{16}$$

where N represents the number of available PIV samples. As can be seen, the time shifts are obtained by translating the pressure signal with respect to the PIV samples. From this estimate of correlation, the above procedure can be applied to form an estimate of transfer function from pressure to velocity: $\tilde{\hat{H}}(\mathbf{x},\omega)$. In the following, we present the maps of the obtained transfer functions for the three first azimuthal pressure modes. We chose specific frequencies that are representative of the low frequency broadband peak, the tonal peaks and the high frequency broadband peak that was observed in the pressure signal. Since $\tilde{H}$ is not normalized, the interpretation of its absolute amplitude has to be driven with care. That is the reason why only relative comparisons of $\tilde{H}$ levels are provided here and that the color scale of those maps was arbitrarily set from zero to the maximum measured value throughout the entire frequency range.

As can be seen in figure 16, in the low frequency part of the spectrum the transfer function from pressure to velocity shows lower amplitude than for other frequencies. Thus, only a small fraction of the pressure fluctuations in that range of frequency signs into the velocity field. This is observable for all the azimuthal modes shown. This confirms that these low frequencies are confined inside the nozzle and are evanescent wave as seen earlier from the pressure PSDs.

On the contrary, as seen in figure 16 at the peak Strouhal number of 0.2 observed in the pressure
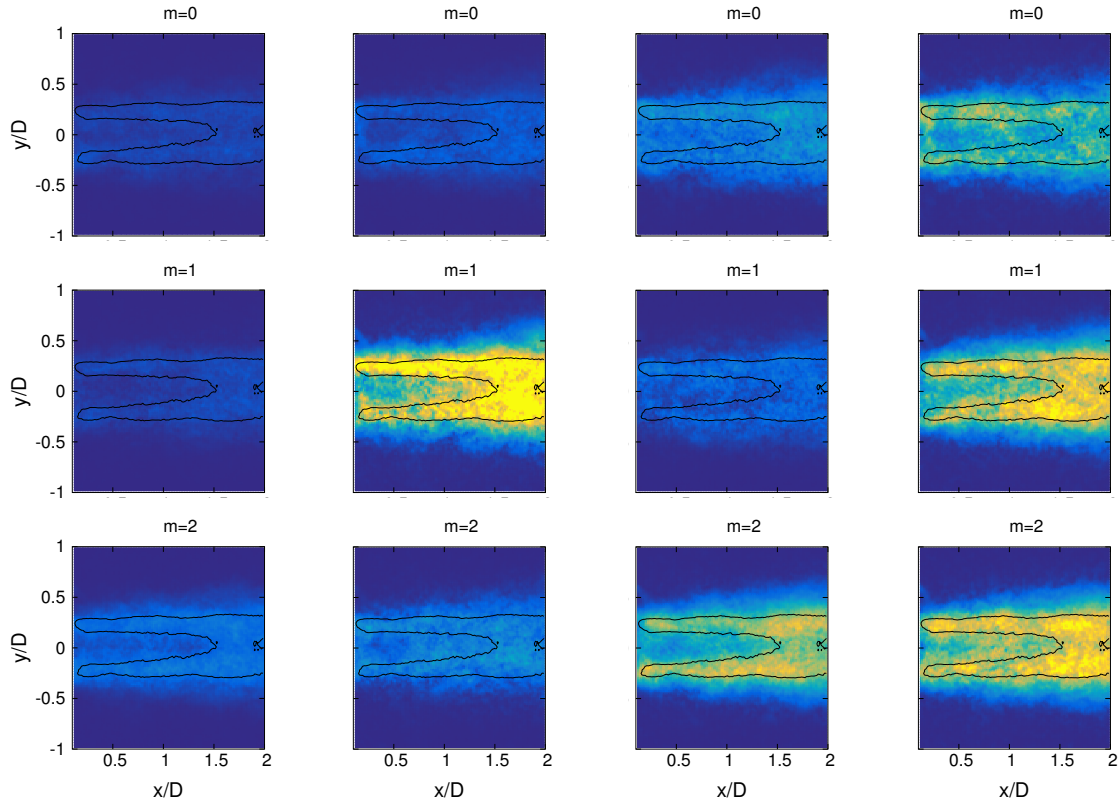
Figure 16. Isocontours of the transfer function magnitude. Each row represent an azimuthal mode of pressure and the columns are for $St = 0.005, 0.2, 0.31, 2.3$ respectively. The black line is the mean velocity iso-contours for $U/U_j = 0.9$. The color scale was arbitrarily set from zero to the maximum measured value throughout the entire frequency range.

spectrum, we clearly see that the pressure azimuthal mode $m = 1$ has a strong signature in the velocity field. Interestingly, this link seems enclosed within the whole high-speed region of the jet, inside the black line representing the iso-contour $U/U_j = 0.9$ in the mean flow. The same observation can be made for $St = 0.31$ from figure 16, where, as expected now, it is the $m = 2$ mode of pressure which signs into the external flow field. This shows that the distinct peaks observed at this NPR are related to perturbations that are present in the jet flow dynamics. It is worth noting that the levels of the transfer function become negligible as soon as the same estimate is based on other Strouhal numbers which are only slightly different from the values corresponding to these peak ones. Since we may expect relatively close energy levels of velocity fluctuations within the external shear layer for such close Strouhal number values in this range, this may thus already indicate a probable non-negligible coherence level between internal pressure and external velocity fluctuations at these frequencies.

In the high frequency region, we see a different behavior. At these frequencies, there is a clear link between the internal pressure and the external flow field. The signature of pressure seems also confined in the high velocity region of the jet, but we see that all the azimuthal modes have

American Institute of Aeronautics and Astronautics

a signature in the velocity field. This conforts the hypothesis that was made previously: the high frequency energetic broadband peak is related to developing instabilities in the mixing layer of the jet.

We have seen that the signature of the pressure into the velocity field is strongly dependent on the pressure azimuthal mode as well as the frequency. Low frequency pressure fluctuations do not seem to contribute to the external flow field, but we have shown that, on the contrary, the strong pressure modes observed inside the nozzle have the clearest signature in the velocity field.

As can be seen in the above figures the pressure signature in the flow field seems confined in the high speed portion of the flow, and the low speed internal flow (*i.e.* at least within the subsonic region downstream of the secondary normal shock wave outside of the nozzle) shows very limited link with the pressure fluctuations. The same comment can be made for all the azimuthal mode of pressure studied here. In other words, the pressure fluctuations in the separated region of the flow do not appear to be directly related only to the separation shock motion, but are rather to be related to instabilities in the shear layer created by the separation of the incoming boundary layer. As mentionned earlier, the aboslute levels $\tilde{H}$ have to be interpreted with care due to the fact that it is not normalized. Moreover, as the PIV is perfomed in the (x, r) plane the velocity field contains contribution of all the azimtuhal velocity modes. The transfer function is hence formed between a given azimtuhal mode of pressure and an ensemble of azimuthal mode of velocity. It is believed that complementary information can probably be extracted by considering time-resolved azimtuhal Fourier modes of velocity as well. This requires a dedicated and far more complicated experiement and is beyond the scope of the present paper.

VII. Conclusion and future work

An experiment has been conducted to investigate the unsteady nature of the pressure and velocity fields of an over-expanded supersonic nozzle flow in FSS regime. We first described the internal pressure field fluctuations in the frequency domain and per azimuthal Fourier modes. Then, the link between the internal pressure and the external velocity fields was investigated through the use of synchronized velocity and pressure measurements. To the best of the author's knowledge, it is the first time that such a methodology is applied for an over-expanded jet flow.

The analysis of the unsteady pressure fields has revealed a complex organisation of the separated region pressure fluctuations. The low frequency modes have been shown to be mostly axisymmetric and confined in the nozzle. The high frequency signature of the developing mixing layer has been identified in the pressure signals and confirmed by its signature in the external velocity field. Highly organised pressure fluctuations both in time and azimuthal direction were described and compared to other references in the literature, suggesting that they are a general feature of the FSS flow regime. It has been found that these organised structures are mainly contained in the anti-symmetric pressure mode so that their contribution to the off-axis loads is obvious. We have

shown that these organized structures are not due to transonic resonance, it is however not clear whether they can be attributed to a screech-like mechanism since they do not radiate tonal sound. Furthermore, we have shown that these tonal dynamics share some features with the instability waves evoked by Tam and Hu [43] and Hu [16], giving a useful insight on what shall be done in the future to completely educe these dynamics. We also found in this study a strong link between the internal pressure and the external velocity field at their frequency, which is also indicating that the origin of these distinct peaks may possibly be found in the jet flow instability itself. As stated in the paper the role of the internal subsonic region of the flow might be of importance. Indeed, it may provide a support for possibly upstream propagative waves that could close a feedback loop, without the need for external screech-like radiated acoustic. Answering these questions requires a dedicated study that is beyond the scope of the present paper.

It was not possible to investigate the numerous peaks observed in the pressure fluctuations at low NPR in this paper. As it has been done for $M_j = 2.09$, the study of their possible link with the external velocity field might give meaningful insights on their nature.

Nevertheless, the results presented in this study provide information about what part of the flow fluctuations should be considered for modelling purposes to predict off-axis loads. It is clear, from the present results, that the low frequency component of the pressure has a poor contribution to these forces. However, we have shown that separated jet and mixing layer dynamics should not be disregarded for this purpose.

Acknowledgments

References

[1] A. Aghababaie and R. Theunissen. Modeling Free Shock Separation Induced Side Loads in Over-expanded Rocket Nozzles. *AIAA Journal*, 53(1):93–103, 2015. ISSN 0001-1452. doi: 10.2514/1. J053014.

[2] M. B. Alkislar, A. Krothapalli, and L. M. Lourenco. Structure of a screeching rectangular jet : a stereoscopic particle image velocimetry study. *Journal of Fluid Mechanics*, 489:121–154, 2003.

[3] W. J. Baars and C. E. Tinney. Transient wall pressures in an overexpanded and large area ratio nozzle. *Experiments in fluids*, 54(2):1–17, 2013.

[4] W. J. Baars, C. E. Tinney, J. H. Ruf, A. M. Brown, and D. M. McDaniels. Wall pressure unsteadiness and side loads in overexpanded rocket nozzles. *AIAA Journal*, 50(1):61–73, 2012. ISSN 0001-1452. doi: 10.2514/1.J051075.

[5] W. J. Baars, J. H. Ruf, and C. E. Tinney. Non-stationary shock motion unsteadiness in an axisymmetric geometry with pressure gradient. *Experiments in Fluids*, 56(5):92, 2015.

[6] P. Carriere, M. Sirieix, and J.-L. Solignac. Similarity properties of the laminar or turbulent separation phenomena in a non-uniform supersonic flow. In *Proceedings of the 12th International Congress of Applied Mechanics, Stanford University, Palo Alto, CA,*, page 145157, 1968.

[7] D. R. Chapman, D. M. Kuehn, and H. K. Larson. Investigation of separated flows in supersonic and subsonic streams with emphasis on the effect of transition. *NACA Rept. 1356*, 1958.

[8] N. T. Clemens and V. Narayanaswamy. Low-frequency unsteadiness of shock wave/turbulent boundary layer interactions. *Annu. Rev. Fluid Mech.*, 46:469–492, 2014.

[9] S. Deck and A. T. Nguyen. Unsteady Side Loads in a Thrust-Optimized Contour Nozzle at Hysteresis Regime. *AIAA journal*, 42(9):1878–1888, 2004. ISSN 0001-1452. doi: 10.2514/1.2425.

[10] J. Délery. *Aérodynamique interne: tuyères et arrières corps*. Ecole nationale supérieure de l'aéronautique et de l'espace, 1998.

[11] G. Dumnov. Unsteady Side-Loads Acting on the Nozzle with Developed Separation Zone. *32nd AIAA/ASME/SAE/ASEE Joint Propulsion Conference and Exhibit*, (July):1–8, 1996.

[12] P. Dupont, C. Haddad, and J. F. Debiève. Space and time organization in a shock-induced separated boundary layer. *Journal of Fluid Mechanics*, 559(1986):255, 2006. ISSN 0022-1120. doi: 10.1017/S0022112006000267.

[13] J. H. Gao and X. D. Li. A multi-mode screech frequency prediction formula for circular supersonic jets. *The Journal of the Acoustical Society of America*, 127(3):1251–1257, 2010.

[14] A. Georges-Picot, A. Hadjadj, and J. Herpe. Influence of downstream unsteadiness on shock pattern in separated nozzle flows. In *50th AIAA/ASME/SAE/ASEE Joint Propulsion Conference*, page 4000, 2014.

[15] G. Hagemann, M. Terhardt, M. Frey, P. Reijasse, M. Onofri, F. Nasuti, and Östlund, J. Flow separation and side-loads in rocket nozzles. *4th International Symposium on Liquid Space Propulsion*, 2000.

[16] F. Q. Hu. The acoustic and instability waves of jets confined inside an acoustically lined rectangular duct. *ICASE Report No. 93-98*, 1993.

[17] M. R. Lammari. *Mesures par vélocimétrie laser doppler dans une couche de mlange turbulente supersonique : quelques aspects du processus de mesure.* PhD thesis, 1996.

[18] C. Y. Loh and K. B. M. Q. Zaman. Numerical investigation of transonic resonance with a convergent-divergent nozzle. *AIAA journal*, 40(12):2393–2401, 2002.

[19] S. Marié, S. Deck, and P. E. Weiss. From pressure fluctuations to dynamic loads on axisymmetric step flows with minimal number of kulites. *Computers & Fluids*, 39(5):747–755, 2010.

[20] L. H. Nave and G. A. Coffey. Sea level side loads in high-area-ratio rocket engines. In *AIAA Paper 73-1284*, 1973.

American Institute of Aeronautics and Astronautics

[21] A. T. Nguyen. *Décollement Instationnaire et Charges Latérales dans les Tuyères Propulsives*. PhD thesis, 2003.

[22] T. D. Norum. Screech suppression in supersonic jets. *AIAA Journal*, 21(2):235–240, 1983.

[23] H. Oertel. Mach wave radiation of hot supersonic jets. In *Mechanics of Sound Generation in Flows*, volume 1, pages 275–281, 1979.

[24] H. Oertel. Mach wave radiation of hot supersonic jets investigated by means of a shock tube and new optical techniques. In *Proceedings of the 12th International Symposium on Shock-Tubes and Waves, Jerusalem*. DTIC Document, 1980.

[25] H. Oertel. Coherent structures producing machwaves inside and outside of the supersonic jet. In *Structure of Complex Turbulent Shear Flow*, pages 334–343. Springer, 1983.

[26] J. Östlund. *Flow processes in rocket engine nozzles with focus on flow separation and side-loads*. PhD thesis, KTH, Stockholm, 2002.

[27] J. Östlund and B. Muhammad-Klingmann. Supersonic flow separation with application to rocket engine nozzles. *Applied Mechanics Reviews*, 58(3):143–177, 2005.

[28] J. Panda. An experimental investigation of screech noise generation. *Journal of Fluid Mechanics*, 378: 71–96, 1999.

[29] S. Piponniau, J. P. Dussauge, J.-F. Debiève, and P. Dupont. A simple model for low-frequency unsteadiness in shock-induced separation. *Journal of Fluid Mechanics*, 629:87, 2009. ISSN 0022-1120. doi: 10.1017/S0022112009006417.

[30] K. J. Plotkin. Shock wave oscillation driven by turbulent boundary-layer fluctuations. *AIAA Journal*, 13(8):1036–1040, 1975.

[31] J. Poggie and A. J. Smits. Experimental evidence for Plotkin model of shock unsteadiness in separated flow. *Physics of Fluids*, 17(1), 2005. ISSN 10706631. doi: 10.1063/1.1833405.

[32] A. Powell. On the mechanism of choked jet noise. *Proceedings of the Physical Society. Section B*, 66 (12):1039, 1953.

[33] G. Raman. Supersonic jet screech: half-century from powell to the present. *Journal of Sound and Vibration*, 225(3):543–571, 1999.

[34] F. Sartor, C. Mettot, R. Bur, and D. Sipp. Unsteadiness in transonic shock-wave/boundary-layer interactions: experimental investigation and global stability analysis. *Journal of Fluid Mechanics*, 781: 550–577, 2015.

[35] F. Scarano. Iterative image deformation methods in piv. *Meas. Sci. Tech.*, 13:R1–R19, 2002.

[36] R. H. Schmucker. Flow process in overexpanded chemical rocket nozzles part 1: Flow separation. *Nasa Tech. Report*, 1973.

[37] R. H. Schmucker. Flow process in overexpanded chemical rocket nozzles part 2: Side loads due to asymetric separation. *Nasa Tech. Report*, 1973.

[38] R. Stark. Flow separation in rocket nozzles - an overview. In *49th AIAA/ASME/SAE/ASEE Joint Propulsion Conference*, 2013.

[39] R. Stark and C. Génin. Flow separation in rocket nozzles under high altitude condition. *Shock Waves*, 27(1):63–68, 2017.

[40] R. Stark and B. Wagner. Experimental study of boundary layer separation in truncated ideal contour nozzles. *Shock Waves*, 19(3):185–191, 2009.

[41] R. H. Stark. Flow separation in rocket nozzles, a simple criteria. In *41st AIAA/ASME/SAE/ASEE Joint Propulsion Conference & Exhibit*, 2005.

[42] P. J. Strykowski, A. Krothapalli, and S; Jendoubi. The effect of counterflow on the development of compressible shear layers. *J. of Fluid Mech.*, 63:1096–1100, 1996.

[43] C. K. W. Tam and F. Q. Hu. On the three families of instability waves of high-speed jets. *Journal of Fluid Mechanics*, 201:447–483, 1989.

[44] C. K. W. Tam, J. M. Seiner, and J. C. Yu. Proposed relationship between broadband shock associated noise and screech tones. *Journal of Sound and Vibration*, 110(2):309–321, 1986.

[45] M. Terhardt, G. Hagemann, and M. Frey. Flow separation and side-load behavious of truncated ideal rocket nozzles. *AIAA Journal*, 2006.

[46] E. Touber and N. D. Sandham. *Low-order stochastic modelling of low-frequency motions in reflected shock-wave/boundary-layer interactions*, volume 671. 2011. ISBN 0022112010005. doi: 10.1017/S0022112010005811. URL http://eprints.soton.ac.uk/178515/.

[47] S. Verma, R. Stark, and H. Oskar. Relation between shock unsteadiness and the origin of side-loads inside a thrust optimized parabolic rocket nozzle. *Aerospace Science and Technology*, pages 474–483, 2006.

[48] S. H. Walker and F. O. Thomas. Experiments characterizing nonlinear shear layer dynamics in a supersonic rectangular jet undergoing screech. *Physics of Fluids (1994-present)*, 9(9):2562–2579, 1997.

[49] J. Westerweel and F. Scarano. Universal outlier detection for piv data. *Experiments in Fluids*, 39(6): 1096–1100, 2005. ISSN 0723-4864. doi: 10.1007/s00348-005-0016-6. URL http://dx.doi.org/10.1007/s00348-005-0016-6.

[50] K. B. M. Q. Zaman, M. D. Dahl, T. J. Bencic, and C. Y. Loh. Investigation of a transonic resonancewith convergent–divergent nozzles. *Journal of Fluid Mechanics*, 463:313–343, 2002.

[51] E. Zukoski. Turbulent boundary-layer separation in front of a forward-facing step. *AIAA journal*, 5: 1746–1753, 1967.